Supporting Information for

Defect-Directed Regeneration of $LiCoO_2$ Cathodes via Gradient Cobalt Reprogramming

Siyu Zhang,[a,b] Yangyang Liu,[c] Gen Chen,[b] Yuping Fan,[d] Hamdy Khamees Thabet,[e] Yu Yao,[f] Zhuoxi Wu,[g] Bingan Lu,[h] Junwei Han,*[a] and Jiang Zhou*[b]

a. School of Minerals Processing and Bioengineering, Central South University, Changsha, Hunan 410083, P. R. China

b. School of Materials Science and Engineering, Hunan Provincial Key Laboratory of Electronic, Packaging and Advanced Functional Materials, Central South University, Changsha, Hunan 410083, P. R. China

c. School of Instrument Science and Technology, Xi'an Jiaotong University, Xi'an, Shaanxi 710049, P. R. China

d. School of Mining Engineering, Taiyuan University of Technology, Taiyuan, Shanxi 030024, P. R. China

e. Center for Scientific Research and Entrepreneurship, Northern Border University, Arar 73213, Saudi Arabia

f. Hefei National Research Center for Physical Sciences at the Microscale, Department of Materials Science and Engineering, University of Science and Technology of China, Hefei, Anhui 230026, P. R. China

g. Department of Mechanical Engineering, The University of Hong Kong, Pokfulam, Hong Kong SAR, 999077, P. R. China

h. School of Physics and Electronics, Hunan University, Changsha, Hunan 410082, P. R. China

*Corresponding authors: zhou_jiang@csu.edu.cn; hanjunwei@csu.edu.cn

Experiment information

Collection of Spent Lithium Cobalt Oxide Cathodes

The spent lithium cobalt oxide (LCO) batteries used in this experiment originate from a company in Hunan, China. The batteries are discharged in brine and then manually disassembled to obtain the cathode sheets. Active materials are separated from the cathode sheets by soaking in N-methyl-2-pyrrolidone combined with ultrasonic heating, yielding the spent cathode material (S-LCO) used in this work. The main chemicals involved in the experimental process and their specifications are as follows: commercial LCO powder ($LiCoO_2$, metal basis, ≥99.5%), ethylene glycol ($C_2H_6O_2$, analytical purity, ≥98%), lithium acetate (CH_3COOLi, metal basis, ≥99.9%), cobalt(II) oxide (CoO, reagent grade, ≥99.9%), magnesium oxide (MgO, analytical purity, ≥98%), conductive carbon black (Super P, analytical purity), and N-methyl-2-pyrrolidone (NMP, electronic grade, ≥99.9%), all purchased from Aladdin Biochemical Technology Co., Ltd. High-voltage LCO material is purchased from dodochem, and lithium metal sheets (14×0.5 mm) and separators (Celgard 2500) are purchased from Canrd.

Regeneration strategy

For materials characterization and coin-cell evaluation, gram-scale regeneration is conducted as follows. First, ethylene glycol and lithium acetate are mixed in a 3:1 molar ratio and heated to 100 ℃ for 20 minutes to form a molten liquid, which serves as the deep eutectic solvent (ELiAc) for this work. Subsequently, S-LCO is added to ELiAc at a ratio of 1 g per 10 mL, and the mixture is stirred at 120 ℃ in a sealed oil bath for 2 hours, followed by solid-liquid separation. The obtained black cathode powder is washed, then mixed with 5 mol% CoO, and annealed at 900 ℃ for 10 hours. The separated ELiAc liquid is directly recovered for subsequent experiments. For the preparation of R-0%-LCO, R-2%-

LCO, and R-8%-LCO, the ELiAc regeneration step remains identical, with the CoO amount added during annealing set to 0%, 2%, and 8%, respectively. The preparation of RHV-LCO involves treating S-LCO with ELiAc, followed by the simultaneous addition of 5 mol% CoO and 0.5 wt% MgO, before annealing at 900 ℃ for 10 hours.

For pouch-cell validation, a 100 g-scale regeneration batch is prepared following the gram-scale procedure described above. The S-LCO/ELiAc ratio is adjusted to 1 g per 2 mL, and the solid precursor mixture is ball-milled at 300 rpm for 1 h before annealing. After annealing, the regenerated product is thoroughly blended and sampled for pouch-cell assembly and electrochemical evaluation.

Material Characterization

The phase composition of the cathode materials is identified using an X-ray diffractometer (Rigaku Mini Flex 600) with a scanning range of 10° to 80° and a step rate of 0.02° s^{-1}. For in situ electrochemical XRD measurements, an ultrathin aluminum foil (0.003 mm) serves as the current collector, with a scan range of 15 °- 25 °. The annealing process of ELiAc is monitored in situ using a high-temperature XRD system (Malvern Panalytical Empyrean), which covers a temperature range from room temperature to 900 ℃ and a scanning angle of 15° to 70°. A differential electrochemical mass spectrometry system (Shanghai Linglu QAS 100) is used to monitor the real-time evolution of oxygen and carbon dioxide gases during the initial battery cycle. The cathode samples are sectioned, and their cross-sectional morphology is examined using a focused-ion-beam scanning electron microscope (TESCAN AMBER X). High-resolution transmission electron microscopy (JEOL JEM-F200) and spherical-aberration-corrected transmission electron microscopy (JEOL ARM 200F) are used to analyze the atomic arrangement and microstructure of the cathode materials. The

stoichiometric ratios of elements in LCO are determined by inductively coupled plasma optical emission spectrometry (PerkinElmer 8300). X-ray photoelectron spectroscopy (Thermo Scientific K-Alpha) is used to analyze the surface elemental valence states and chemical composition of the cathode. The molecular structure and functional group information of ELiAc and its components are characterized using Fourier transform infrared spectroscopy (Thermo Scientific Nicolet iS 10) and liquid nuclear magnetic resonance spectroscopy (Bruker AVANCE 400).

Electrochemical Testing

The cathode slurry consists of active material (80 wt%), conductive carbon black (10 wt%), and polyvinylidene fluoride binder (10 wt%). These components are thoroughly ground and mixed in a mortar. Afterward, N-methyl-2-pyrrolidone is added, and the grinding continues for approximately 10 minutes to form a homogeneous slurry. The slurry is then coated onto an aluminum foil current collector and processed in an 80 ℃ vacuum drying oven for over 12 hours. The dried electrode sheets are punched into 12 mm-diameter disks, with the active material areal density controlled between 1.5 and 3.0 mg cm^{-2}. A CR2025 coin-cell assembly is used in the test system, featuring a lithium metal foil anode and an electrolyte containing 1 mol/L LiPF6 in a DMC/EC/EMC mixed solvent. Battery assembly is completed in a glove box (MIKROUNA, H_2O < 0.1 ppm, O_2 < 0.1 ppm). For pouch-cell fabrication, the R-LCO cathode slurry is prepared using active material, polyvinylidene fluoride, Super P conductive carbon, and carbon nanotubes at a mass ratio of 96.5:1.5:1.0:1.0, while the graphite anode slurry consists of graphite, carboxymethyl cellulose, Super P conductive carbon, and styrene-butadiene rubber at a mass ratio of 94.5:1.5:1.5:2.5. The cathode and anode coating areal densities are 11.00 ± 0.22 and 6.36 ± 0.18 mg cm^{-2}, respectively, with the N/P ratio controlled at 1.1. The assembled R-

LCO//graphite pouch full cells are evaluated at 25 °C. Cycling performance and rate capability tests are conducted using a Neware battery test system (NEWARE, MIHW-200-160CH-B), with voltage windows set to 3.0–4.3 V, 3.0–4.5 V, and 3.0–4.6 V, and test rates including 0.2 C, 0.5 C, 1 C, 2 C, and 4 C (1 C = 270 mAh g^{-1}). Cyclic voltammetry and electrochemical impedance spectroscopy measurements are performed using a Shanghai Chenhua CHI660E electrochemical workstation and a Wuhan Corrtest CS350M test system, respectively.

Theoretical Calculation

All first-principles calculations in this study are carried out using the Vienna Ab initio Simulation Package (VASP) within the PBE-GGA functional, augmented by the DFT+U approach to account for on-site Coulomb interactions of Co 3d electrons. A Hubbard U-J value of 3.3 eV is applied for Co. Electron-ion interactions are described with the projector augmented-wave (PAW) method, and a plane-wave energy cutoff of 520 eV is adopted. For LCO-type systems, a $2 \times 2 \times 1$ k-point mesh is used during structural relaxation, while a $3 \times 3 \times 2$ mesh is employed for self-consistent energy calculations. For CoO systems, the corresponding k-point grids are $2 \times 2 \times 2$ and $3 \times 3 \times 3$, respectively. During geometry optimization, the convergence threshold for the electronic self-consistent field (SCF) cycle is set to 10^{-5} eV per atom, while a stricter criterion of 10^{-6} eV per atom is used for static energy calculations. Atomic positions are relaxed until the residual forces fall below 0.02 eV/Å. The migration of Co ions proceeds from an initial octahedral site, passes through an intermediate site, and ultimately reaches a Li site. The atomic configurations corresponding to each characteristic site along the path are extracted, and the relative energy of each site is calculated with reference to the initial site energy using the formula $\Delta E_{site} = E_{site} - E_{initial}$. The binding energy of the

repair agent ELiAc with Li^+ and Co^{2+} is calculated based on the total energy difference between the bound state and the isolated components. To assess the structural stability of the material in the delithiated state, the Gibbs free energy change (ΔG) of the corresponding defect-forming reaction is evaluated. For $Li_9Co_{27}O_{54}$, the process follows:

$$Li_9Co_{27}O_{54} \rightarrow Li_9Co_{27}O_{53} + \frac{1}{2}O_2 \tag{1}$$

The enthalpy change (ΔH) of the reaction is calculated as:

$$\Delta H = \frac{E(Li_9Co_{27}O_{53}) + \frac{1}{2}E(O_2) - E(Li_9Co_{27}O_{54})}{0.5} \tag{2}$$

Here, $E(O_2)$ and $E(^{Li_9Co_{27}O_{54}})$ denote the total energies of the O_2 molecule and the pristine $Li_9Co_{27}O_{54}$ system, respectively, and $E(^{Li_9Co_{27}O_{53}})$ is the total energy of the defective structure obtained after removing the oxygen atom possessing the smallest Bader charge from $Li_9Co_{27}O_{54}$ followed by structural relaxation. An analogous procedure is applied to the $Co_{27}O_{27}$ system. Under standard conditions (1 bar, 298 K), the entropy contribution of gaseous O_2 ($-T\Delta S = -0.63$ eV) is incorporated to obtain ΔG.

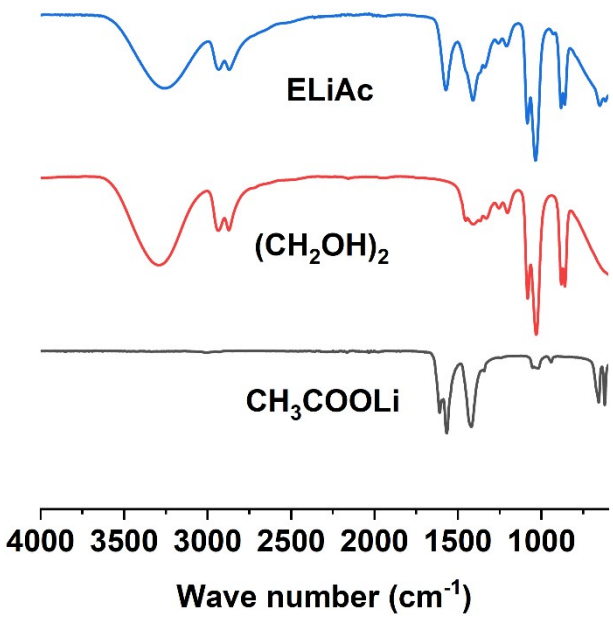

Fig. S1 FTIR spectra of lithium acetate, ethylene glycol, and the resulting ELiAc complex.

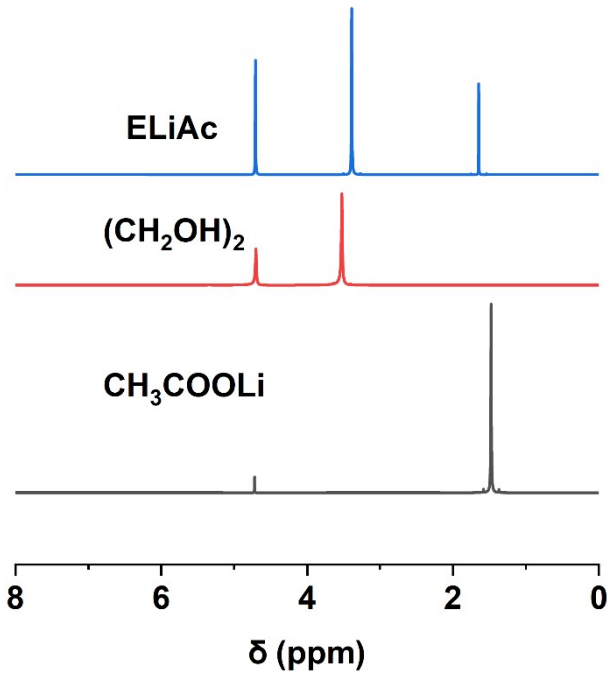

Fig. S2 ^{1}H NMR spectra of lithium acetate, ethylene glycol, and the resulting ELiAc complex.

$$-(CH_2\text{-}CF_2)_n- + -OH \longrightarrow -(CH{=}CF)_n- + H_2O + -F$$

$$-(CF_2CH{=}CF)_n- + -2OH \longrightarrow -(CF{=}CHCO)_n- + H_2O + -2F$$

Fig. S3 Schematic diagram of the reaction mechanism for PVDF binder removal by ELiAc.

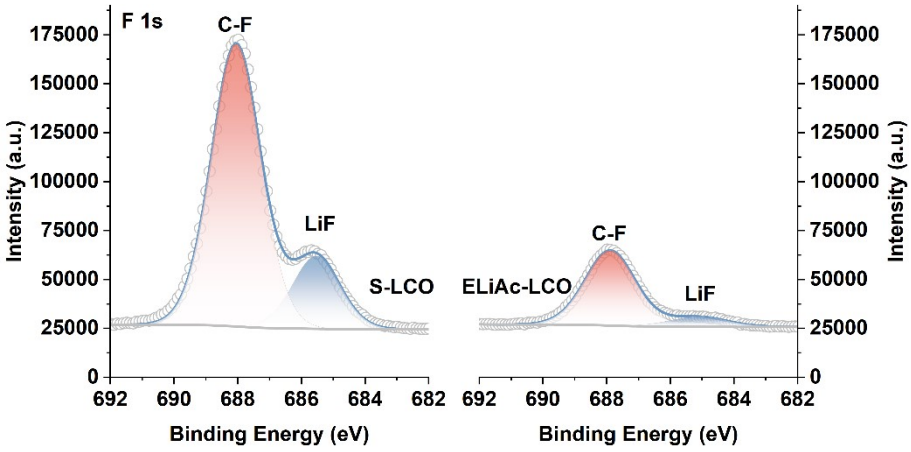

Fig. S4 F 1s XPS spectra of S-LCO and ELiAc-LCO.

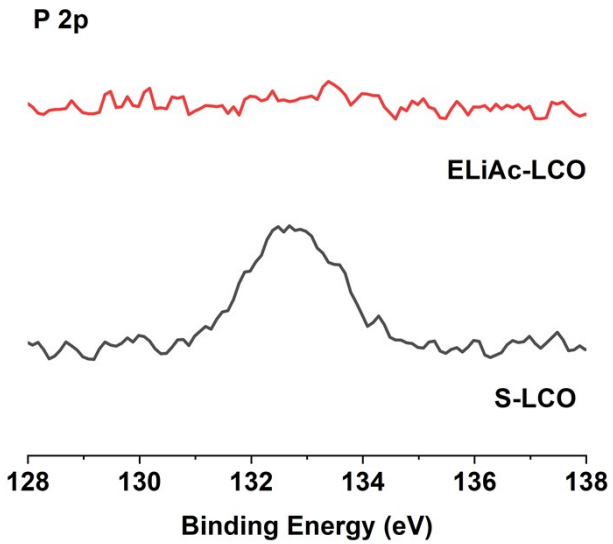

Fig. S5 P 2p XPS spectra of S-LCO and ELiAc-LCO.

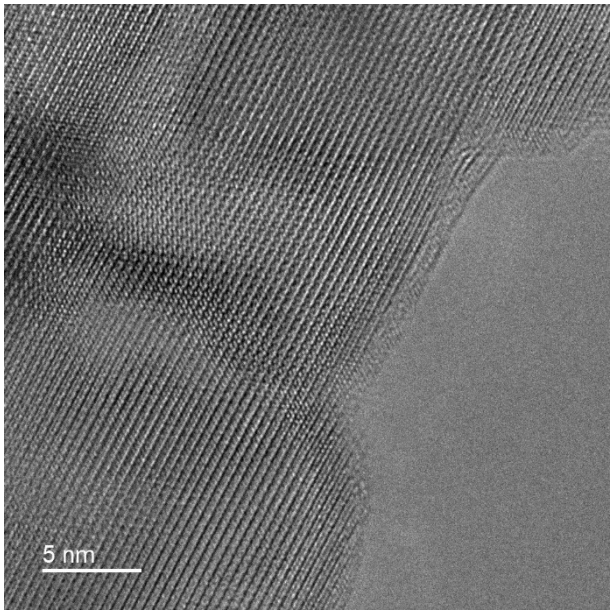

Fig. S6 HRTEM image of ELiAc-LCO.

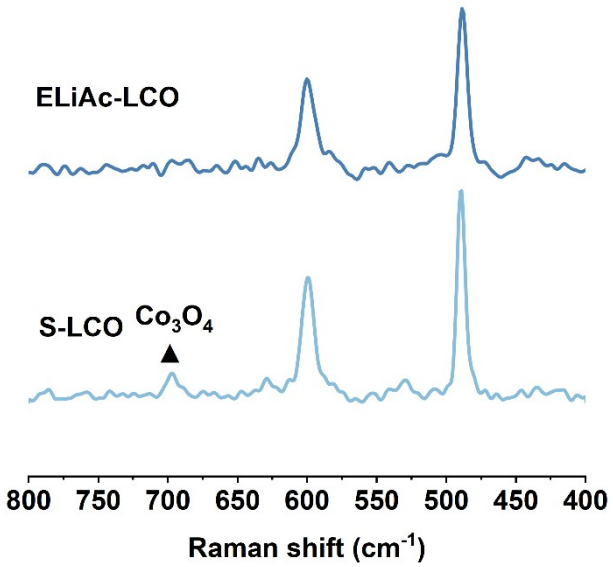

Fig. S7 Raman spectra of S-LCO and ELiAc-LCO.

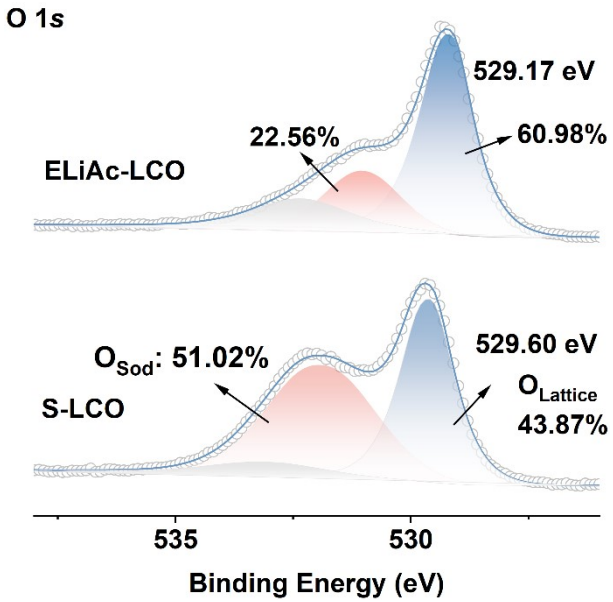

Fig. S8 O 1s XPS spectra of S-LCO and ELiAc-LCO.

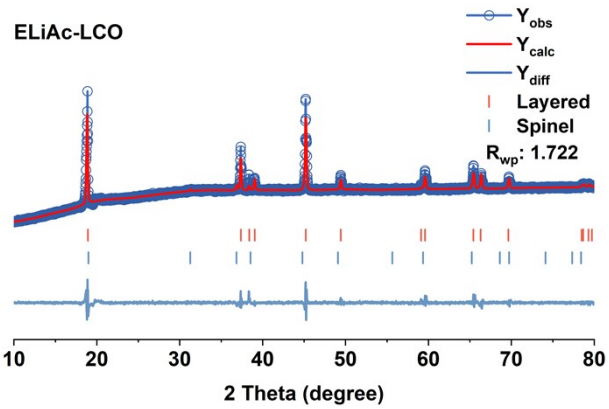

Fig. S9 Rietveld refinement XRD pattern of ELiAc-LCO.

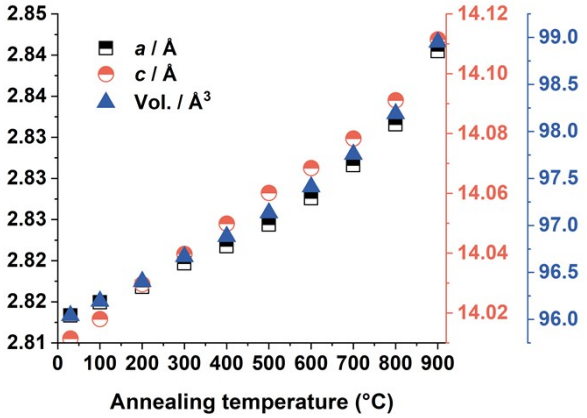

Fig. S10 Evolution of Lattice Parameters and Unit Cell Volume of LCO during Annealing.

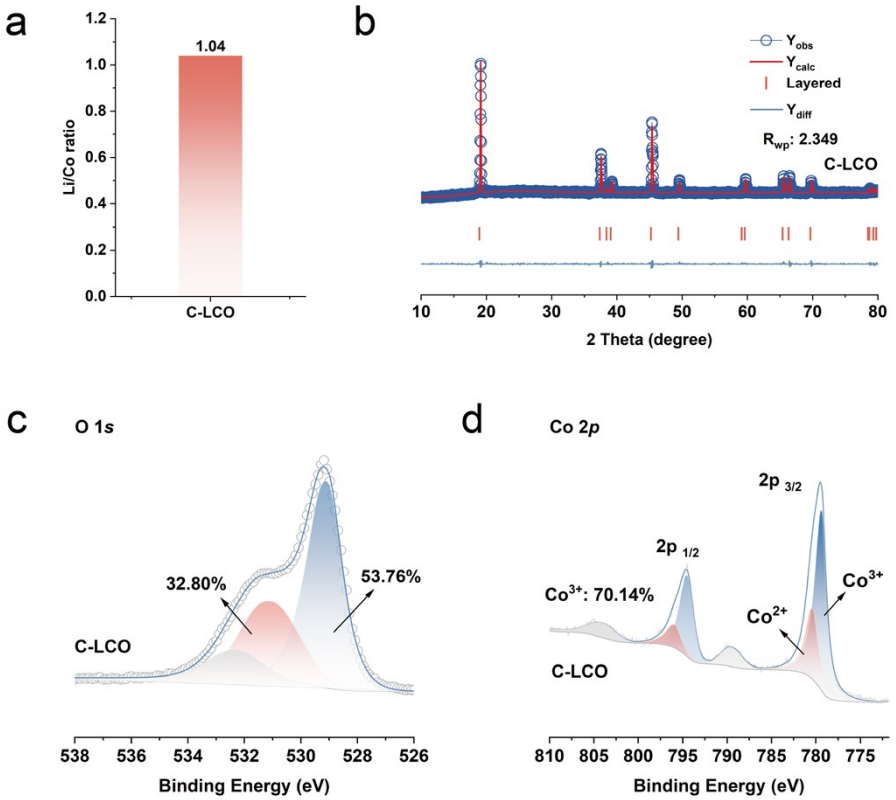

Fig. S11 (a) Li/Co molar ratio of C-LCO determined by ICP-OES. (b) Rietveld refinement of the XRD pattern of C-LCO. (c) O 1s XPS spectrum of C-LCO. (d) Co 2p XPS spectrum of C-LCO.

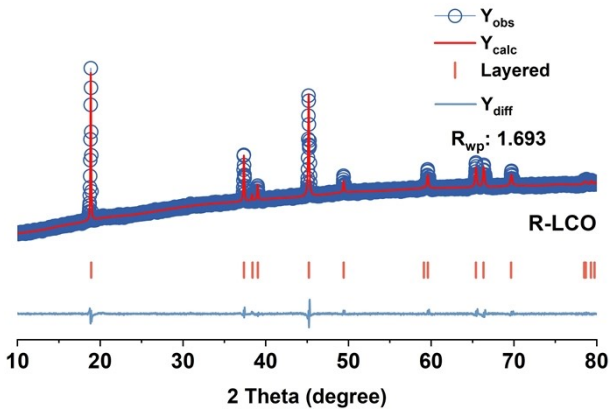

Fig. S12 Rietveld refinement XRD pattern of R-LCO.

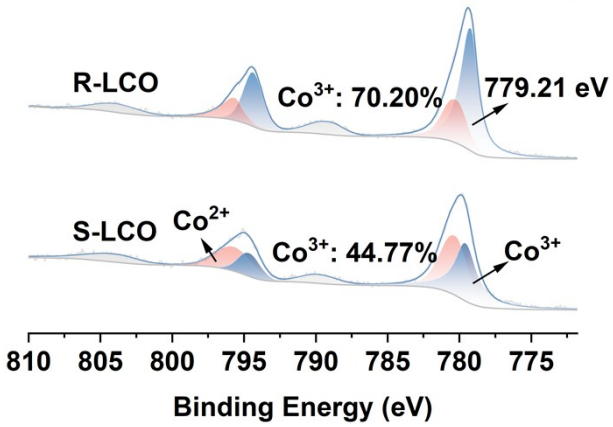

Fig. S13 Co 2p XPS spectra of S-LCO and R-LCO.

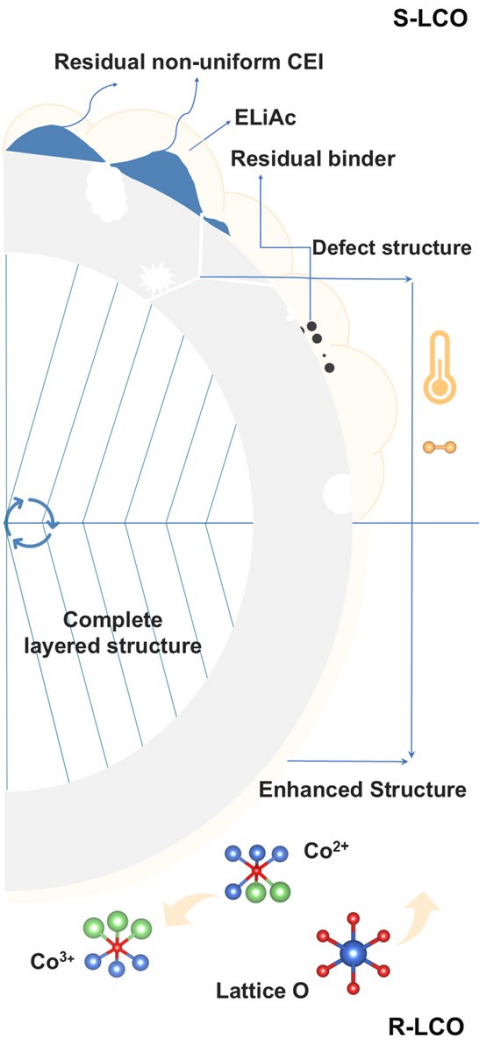

Fig. S14 Schematic diagram of composition and structural remodeling in LCO.

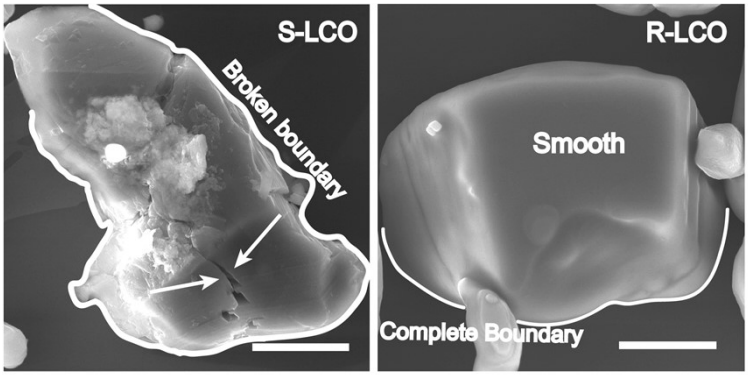

Fig. S15 SEM images of S-LCO and R-LCO (Scale bar = 5 μm).

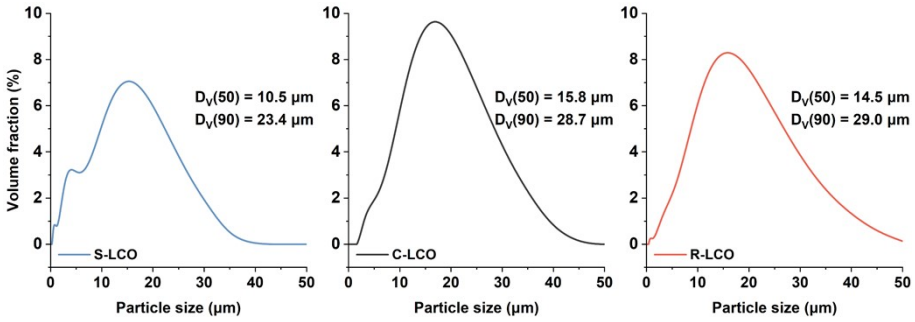

Fig. S16 Particle size distributions of S-LCO, C-LCO, and R-LCO.

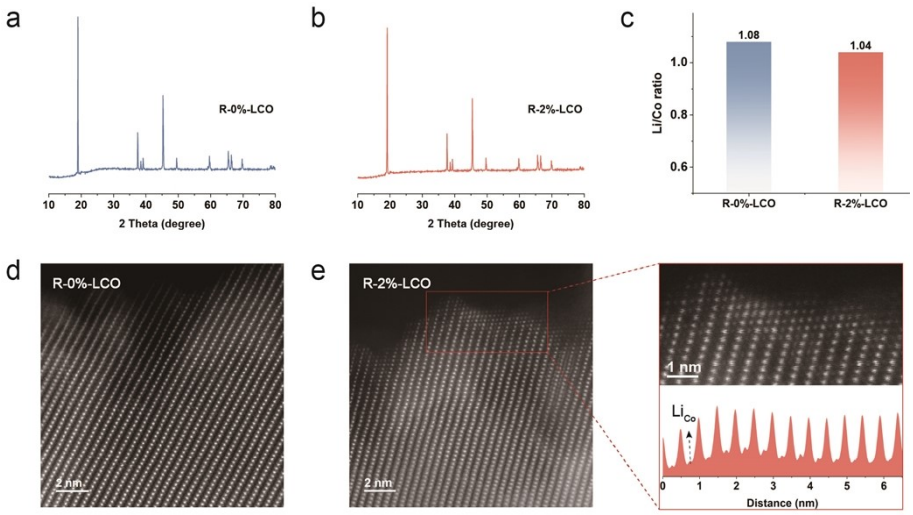

Fig. S17 (a, b) XRD patterns of R-0%-LCO and R-2%-LCO. (c) ICP-OES analysis of LCO with different CoO contents. (d, e) STEM images of R-0%-LCO and R-2%-LCO.

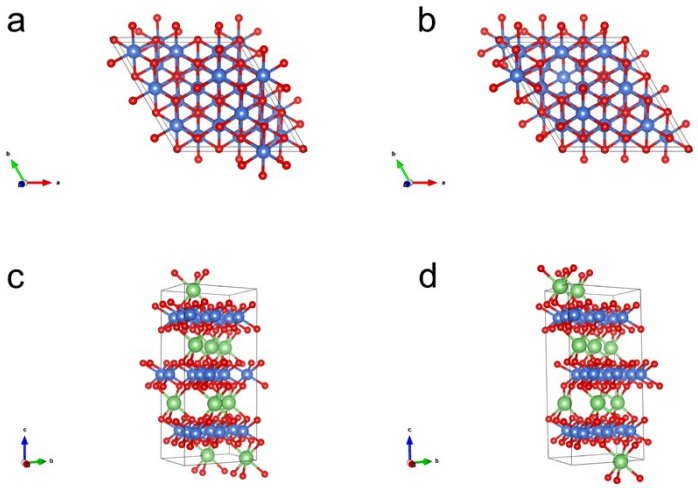

Fig. S18 Interface structures of (a, b) R-LCO and (c, d) C-LCO at 66% delithiation.

(a) $Co_{27}O_{27}$ and (c) $Li_9Co_{27}O_{54}$ are the stoichiometric models.

(b) $Co_{27}O_{26}$ and (d) $Li_9Co_{27}O_{53}$ are the corresponding models with an oxygen vacancy.

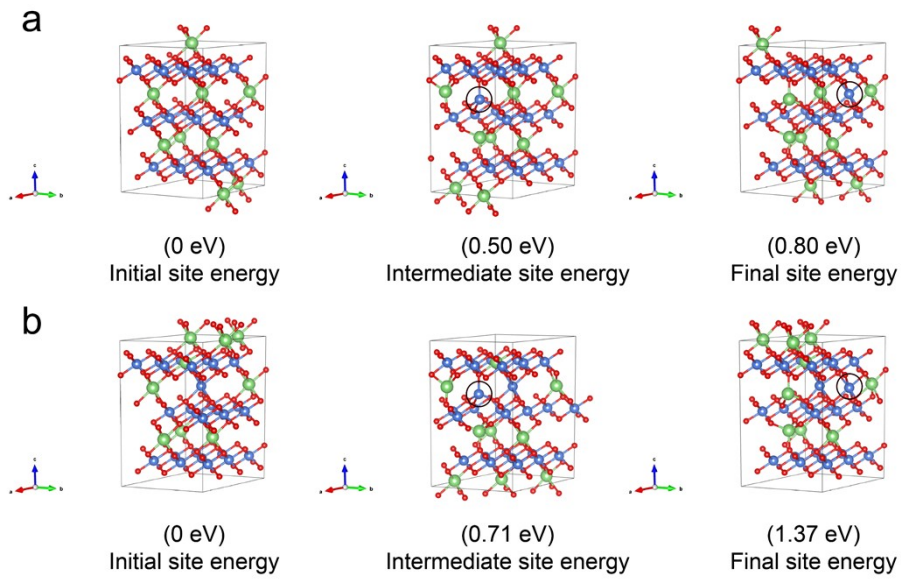

Fig. S19 Relative energy for Co migration from the transition-metal layer to a Li-layer site within the sub-interface structures of (a) C-LCO and (b) R-LCO at 66% delithiation.

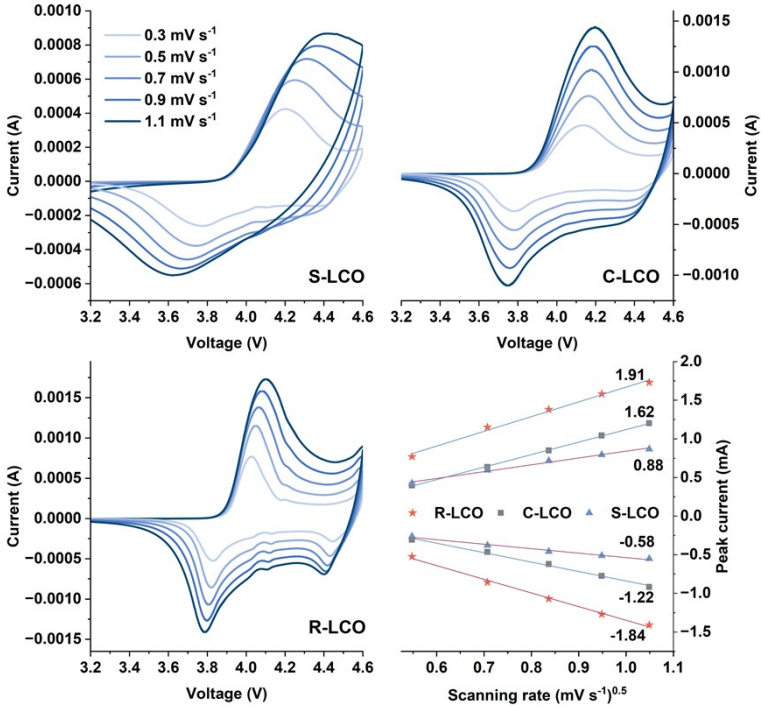

Fig. S20 CV curves at different scan rates and the linear relationship between the oxidation/reduction peak currents and scan rates.

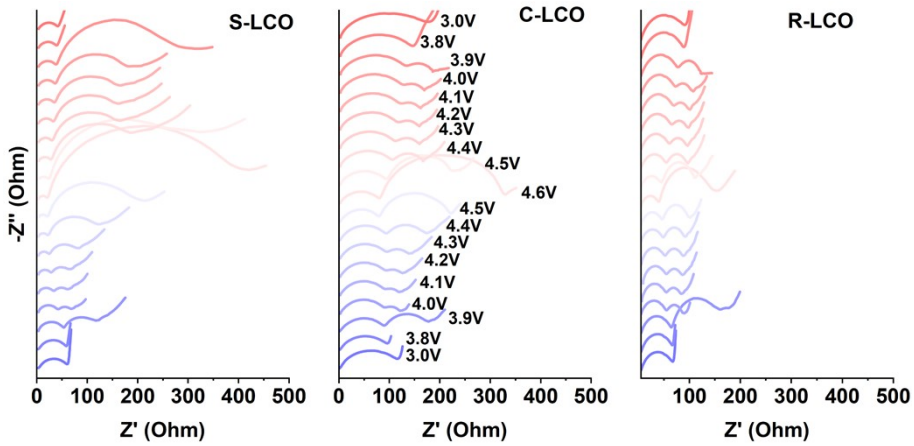

Fig. S21 In situ EIS measurements of S-LCO, C-LCO, and R-LCO.

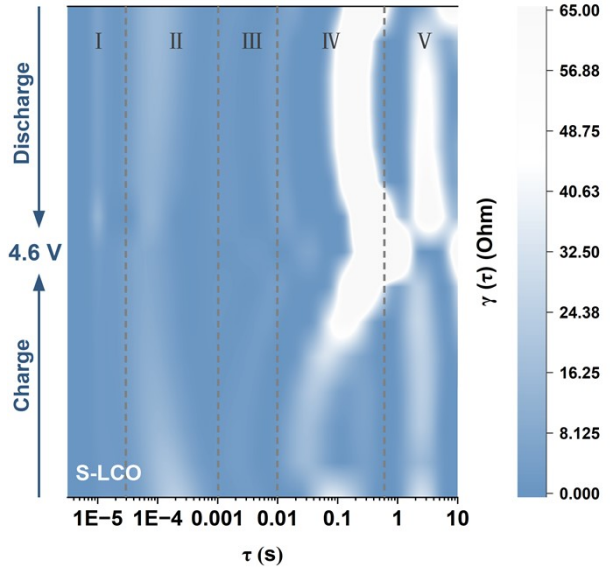

Fig. S22 In situ DRT spectra of S-LCO (3.9–4.6 V).

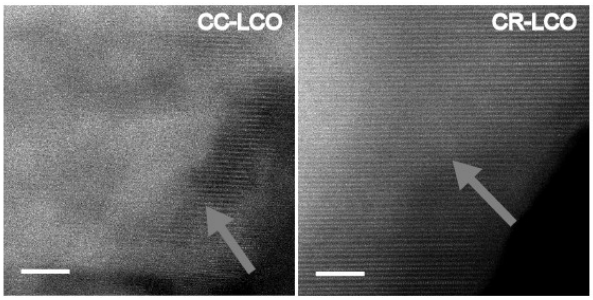

Fig. S23 HAADF-STEM images of CC-LCO and CR-LCO (Scale bar = 5 nm).

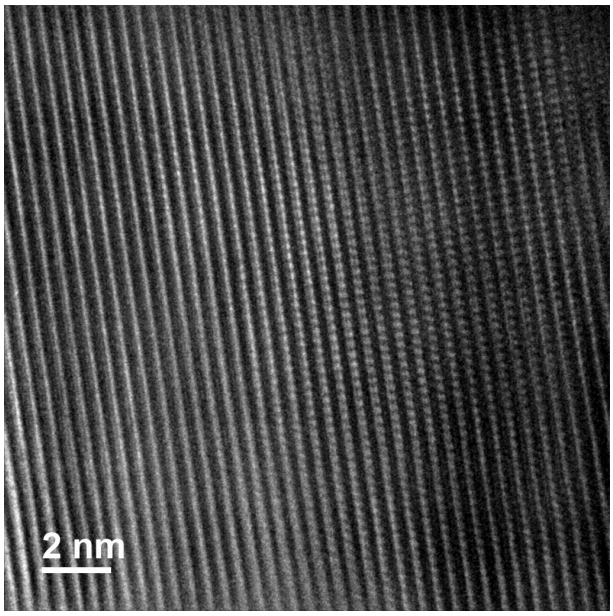

Fig. S24 HRTEM image of CR-LCO.

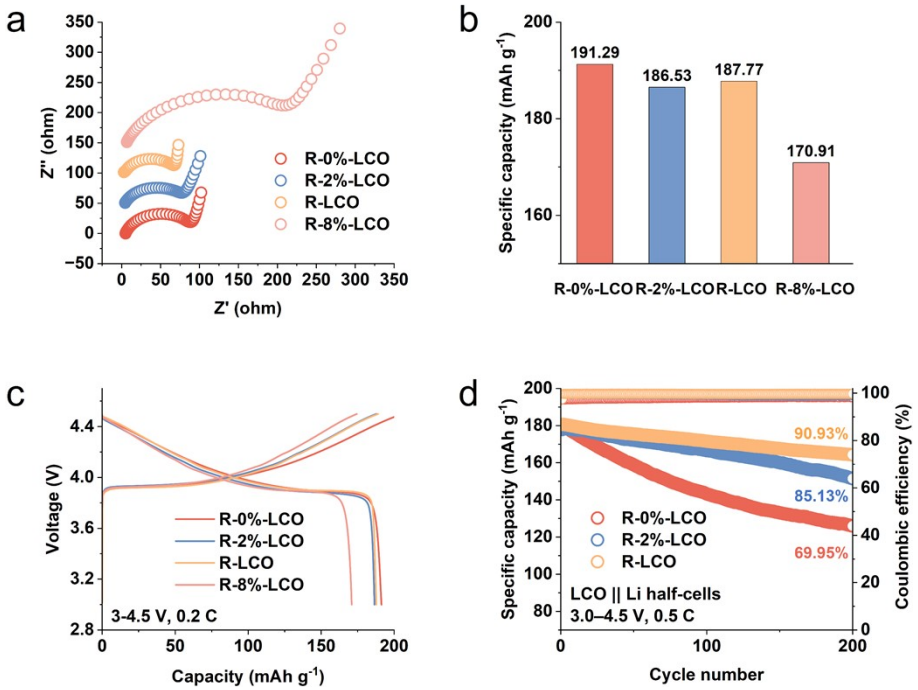

Fig. S25 (a) Nyquist plots of regenerated LCO with different CoO contents. (b) Discharge capacities of regenerated LCO with different CoO contents (0.2 C, 3.0–4.5 V). (c) Charge–discharge profiles at 0.2 C within 3.0–4.5 V. (d) Cycling performance.

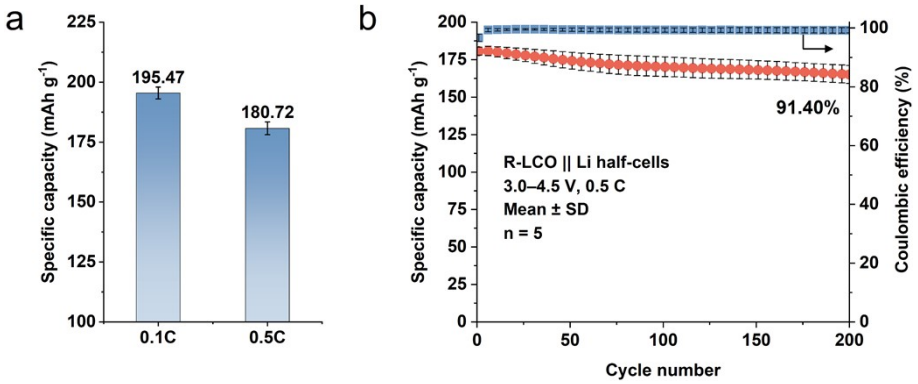

Fig. S26 (a) Average discharge capacities of R-LCO||Li half-cells at different rates. (b) Averaged cycling performance and Coulombic efficiency.

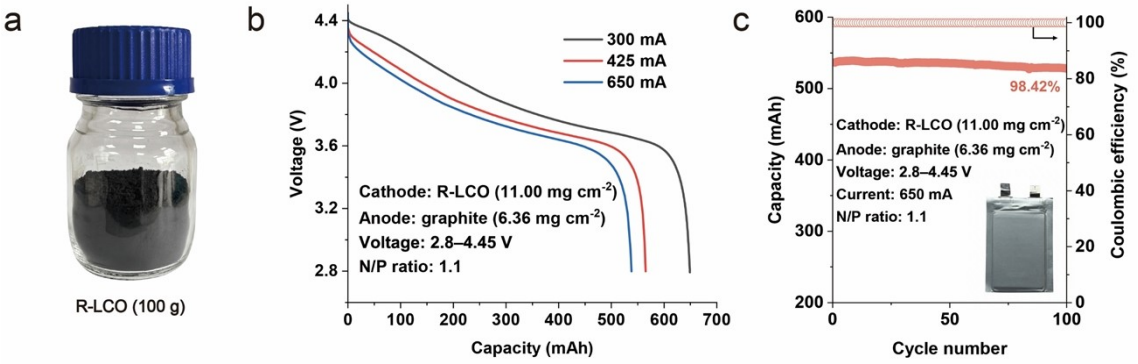

Fig. S27 (a) Photograph of 100 g-scale R-LCO. (b) Discharge profiles and (c) cycling performance of the R-LCO//graphite pouch full cell.

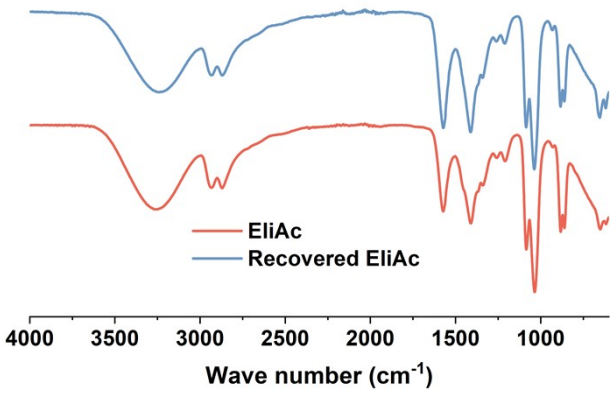

Fig. S28 FTIR spectra of ELiAc and recovered ELiAc.

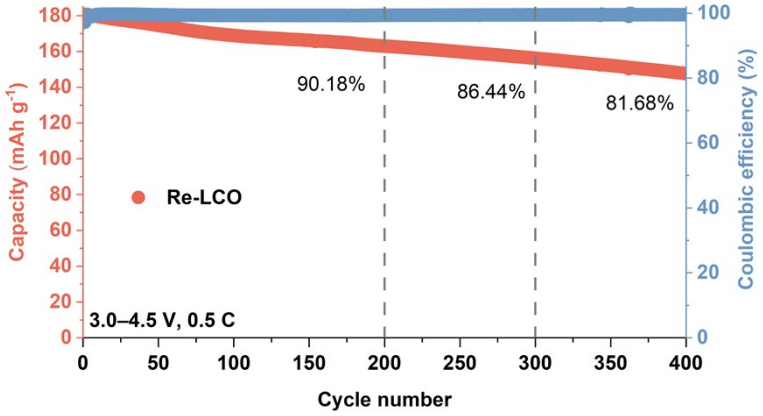

Fig. S29 Long-term cycling performance of Re-LCO.

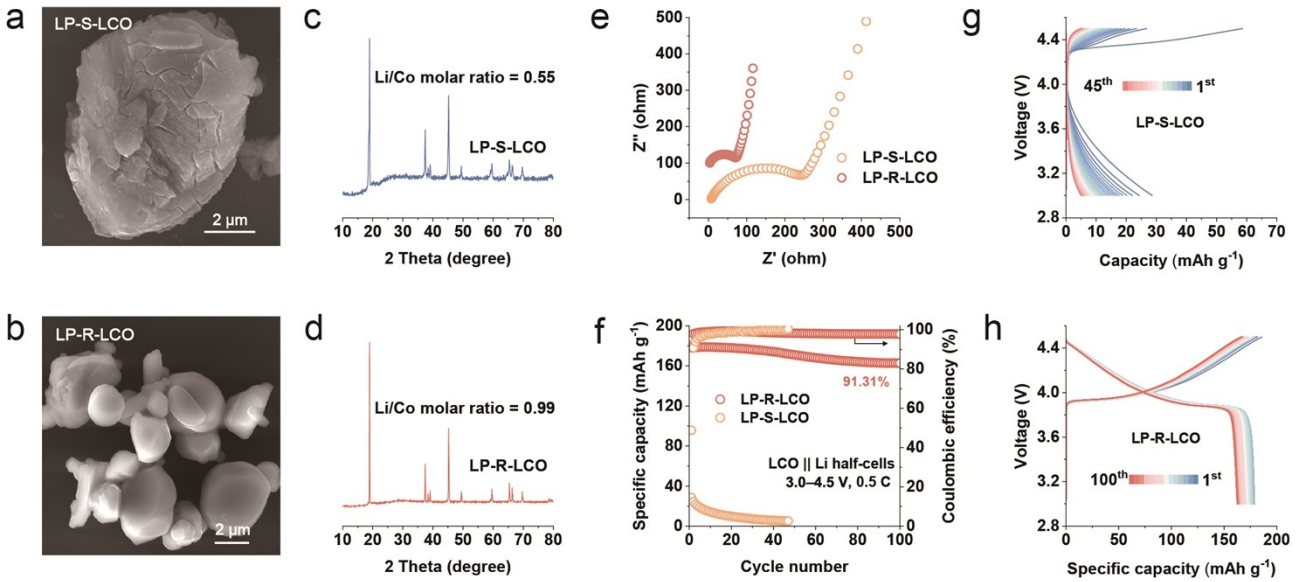

Fig. S30 (a, b) SEM images of LP-S-LCO and LP-R-LCO. (c, d) XRD patterns and Li/Co molar ratios. (e) Nyquist plots. (f) Cycling performance. (g, h) Charge–discharge profiles during cycling. LP-S-LCO and LP-R-LCO denote Li-poor spent LCO and regenerated Li-poor LCO, respectively.

Table S1 Lattice parameters and disorder-associated Li/Co site occupancies derived from Rietveld refinement of XRD patterns for S-LCO, ELiAc-LCO, R-LCO, and C-LCO

Samples	a (Å)	c (Å)	Co_{Li} (%)	Li_{Co} (%)
S-LCO	2.8111	14.03295	15.13	3.09
ELiAc-LCO	2.80914	14.02138	8.97	3.34
R-LCO	2.81867	14.07331	4.85	2.37
C-LCO	2.81754	14.06502	0.46	0.46

Table S2 Preprocessing throughput metrics

	Feedstock	Tonnage (t/yr)	Location
S-LCO	Black mass	10000	China

Note: This study selects conventional industrialized processes and representative technological advancements as evaluation subjects in its economic and technical analysis. Economic calculations occur based on different material flow pathways, while energy consumption and GHG emissions are computed using the Everbatt 2023 model. In the Hydro-DES process, the choline chloride to oxalic acid molar ratio is set at 1:1. Their quantities are determined based on the theoretical requirements for complete reaction with S-LCO. Within this process, choline chloride is designed for three reuse cycles, with a 25% loss rate per cycle. In the ELiAc-driven DR strategy, the required lithium acetate dosage is first determined based on the theoretical lithium deficiency in S-LCO, from which the total ELiAc demand is calculated. Considering potential discrepancies between theoretical and actual lithium replenishment in practice and uncertainties in S-LCO's spent condition in industrial settings, the actual ELiAc usage is ultimately set at 300% of the theoretical value to ensure full reaction coverage.

Table S3 Prices of raw materials and products in the techno-economic analysis

Materials	Price (US$ t^{-1})
Black mass	12428
Lithium acetate	18620
Sulfuric acid	82.2
Soda ash	205.5
Cobalt (II) oxide	64630
Hydrogen peroxide	252.72
Cobalt hydroxide	36927
Ethylene glycol	563.6
Lithium carbonate	10495
Choline chloride	758.6
Oxalic acid	303
Cobalt oxalate dihydrate	18621
Sodium hydroxide	351
LCO (4.5 V)	51724

Note: Data are obtained from the Shanghai Nonferrous Metals Network (https://hq.smm.cn/), the China Nonferrous Metals Network (https://www.cnmn.com.cn/), and the China Chemical Network (https://www.chinachemnet.com/).

Table S4 Cost breakdown for different recycling processes (US$ kg^{-1})

	Hydro-DES	Hydro	Pyro	Direct
Black mass	12.43	12.43	12.43	12.43
Annualized capital cost	0.7	0.72	1.17	1.17
Other fixed costs	0.13	0.19	0.19	0.19
Plant overhead	0.14	0.14	0.14	0.14
Maintenance	0.11	0.12	0.19	0.19
Labor	0.03	0.03	0.03	0.03
Other variable costs	0.07	0.04	0.02	0.02
Utilities	0.07	0.10	0.12	0.14
Materials	2.27	0.53	0.36	3.70